Published in final edited form as:
J Magn Reson. 2012 August ; 221: 129–138. doi:10.1016/j.jmr.2012.05.007.

Phase-Contrast MRI and CFD Modeling of Apparent ^{3}He Gas Flow in Rat Pulmonary Airways

Kevin R. Minard[*], **Andrew P. Kuprat**, **Senthil Kabilan**, **Richard E. Jacob**, **Daniel R. Einstein**, **James P. Carson**, and **Richard A. Corley**
Pacific Northwest National Laboratory, P.O. Box 999, Richland, WA 99352

Abstract

Phase-contrast (PC) magnetic resonance imaging (MRI) with hyperpolarized ^{3}He is potentially useful for developing and testing patient-specific models of pulmonary airflow. One challenge, however, is that PC-MRI provides apparent values of local ^{3}He velocity that not only depend on actual airflow but also on gas diffusion. This not only blurs laminar flow patterns in narrow airways but also introduces anomalous airflow structure that reflects gas-wall interactions. Here, both effects are predicted in a live rat using computational fluid dynamics (CFD), and for the first time, simulated patterns of apparent ^{3}He gas velocity are compared with in-vivo PC-MRI. Results show 1) that correlations (R^2) between measured and simulated airflow patterns increase from 0.23 to 0.79 simply by accounting for apparent ^{3}He transport, and 2) that remaining differences are mainly due to uncertain airway segmentation and partial volume effects stemming from relatively coarse MRI resolution. Higher-fidelity testing of pulmonary airflow predictions should therefore be possible with future imaging improvements.

Keywords

^{3}He MRI; CFD; Pulmonary Airflow; Convection-Diffusion

1. Introduction

Computational fluid dynamics (CFD) provides a quantitative basis for predicting respiratory airflow and inhaled material transport [1]. Since both depend intimately on airway shape and curvature [2], modern CFD often employs anatomical imaging for rapidly compiling realistic descriptions of airway geometry [3,4]. Predicted transport, however, is so detailed that new experimental methods are needed to assess simulation results [5]. Phase-contrast (PC) magnetic resonance imaging (MRI) with hyperpolarized ^{3}He is particularly promising since it has already been successfully applied for visualizing respiratory airflows in rats [6] and humans [7]. This is especially important for inhalation toxicology given the rat's widespread use as a human surrogate for safety testing, and the established role of CFD for relating airborne exposure from one species to another [8].

[*]**Corresponding Author:** Kevin R. Minard, Pacific Northwest National Laboratory, P.O. Box 999, MSIN J4-18, Richland, WA 99352, Phone: (509) 371-6897, Fax: (509) 371-6946, kevin.minard@pnnl.gov.

During PC-MRI, pulsed magnetic field gradients make acquired data sensitive to all types of transport, including gas diffusion [9]. This is particularly challenging when comparing PC-MRI to CFD since rapid gas diffusion blurs laminar flow structure in measured results [6,10]. Physically, this occurs when gas diffuses across shear-induced velocity gradients and excited nuclei traverse different laminar flow steams during raw data collection. In straight pipes this process has been described analytically, and predicted patterns of measured airflow have been experimentally validated [6]. Results show explicitly how ^{3}He PC-MRI provides apparent values of local gas velocity that not only depend on actual airflow but also on the rate of gas diffusion and underlying imaging parameters [6]. No general approach, however, has yet been described for predicting apparent velocity in more complex airway geometry.

In typical respiratory CFD, mass transfer from flow and diffusion is predicted by solving the Navier-Stokes and convection-diffusion equations [11]. Here, a similar approach is utilized for generally describing the combined influences of flow and diffusion on ^{3}He PC-MRI. To benchmark CFD predictions, simulated values for apparent ^{3}He transport in straight tubes are first shown to agree with previous analytical results. Validated CFD approaches are then applied to carry out the first ever comparison between measured and predicted airflow patterns in rat pulmonary airways. Findings not only demonstrate the integrated use of ^{3}He PC-MRI for developing and assessing predicted airflow in-vivo, but also for testing the mass-transfer models that are fundamental to gas mixing in respiratory physiology.

2. Theory

2.1. Apparent Gas Velocity (v_{app})

PC-MRI for this study is shown in Fig. 1. During raw data collection pulsed magnetic field gradients encode gas motion and location. Motion is encoded first using a bipolar gradient waveform that can be applied along any orthogonal imaging axis (j). Shortly after, spatial location along the z-axis is registered using standard phase encoding, whereas radial position in the xy-plane is frequency-encoded. To measure each vector component of apparent gas velocity ($\boldsymbol{v}_{app}^{j}$), four separate three-dimensional (3D) images are acquired. One reference image is collected with no motion encoding, and each of the others is collected with motion encoding gradients applied along a different axis. Apparent gas velocity at each image location $\boldsymbol{r_0}$ is then calculated using the known motion sensitivity (α_j) and the relative difference in MRI signal phase (Φ_j), such that [6] –

$$\boldsymbol{v}_{app}^{j}(\boldsymbol{r}_{\mathbf{o}}) = \frac{\Phi_j(\boldsymbol{r}_{\mathbf{o}})}{\alpha_j} = \frac{\theta_j - \theta_0}{\alpha_j}. \quad (1)$$

Here, θ_0 represents the measured phase for spatially resolved MRI signal in the reference image, θ_j is the phase when motion encoding is along the j-axis, and motion sensitivity (α_j) is determined by the time-dependent amplitude for motion encoding gradients ($G_j(t)$) and the gyromagnetic ratio (γ= 20376 radian Gauss^{-1} s^{-1}) [9] –

$$\alpha_j = \gamma \int t G_j(t) dt. \quad (2)$$

For the bipolar waveform in Fig. 1, $\alpha_j = \gamma G_j \delta\Delta$ - where G_j is the gradient pulse amplitude (Gauss cm^{-1}), δ is the pulse duration, and Δ is their leading-edge separation time.

Equation 1 recognizes that molecular motion alters the relative phase (Φ_j) of local MRI signal in images collected using different motion encoding [9]. If each molecule's instantaneous location is denoted by $\boldsymbol{r}(t)$, statistical analysis shows that relative changes

induced by a large number of molecules can be described in terms of an ensemble average ($\langle\rangle$) over all gas encoded at a given image location $\boldsymbol{r_0}$ [6,12] –

$$\Phi_j(\boldsymbol{r}_\mathbf{o})=\gamma\int G_j(t)\left\langle \boldsymbol{r}_j(t)\right\rangle dt. \tag{3}$$

Mathematically, this describes how relative changes in image phase (Φ_j) depend on motion-encoding gradients (G_j(t)) and average gas motion along their applied direction $\langle \boldsymbol{r}_j(t)\rangle$. Combining results from Eqs. 1–3 then gives a more convenient expression for apparent gas velocity measured in Fig. 1 –

$$\boldsymbol{v}^j_{app}(\boldsymbol{r}_\mathbf{o})=\frac{1}{\delta\Delta G_j}\int G_j(t)\left\langle \boldsymbol{r}_j(t)\right\rangle dt. \tag{4}$$

In classical PC-MRI analysis it is traditionally assumed that - 1) all molecules contributing to the localized MRI signal undergo constant flow at some velocity $\boldsymbol{v}$, and 2) flow does not carry molecules outside of resolved volume elements during different encoding events. In this case, $\left\langle \boldsymbol{r}_j(t)\right\rangle=\boldsymbol{r}^j_\mathbf{o}+\boldsymbol{v}_j t$, and it is seen from Eq. 4 that $\boldsymbol{v}^j_{app}(\boldsymbol{r}_\mathbf{o})=\boldsymbol{v}_j$. More generally, if motion is not constant, the same equation correctly describes the time averaging inherent to PC-MRI [6]. There is also no necessary assumption about molecules remaining in resolved volumes since the ensemble average is strictly over only those molecules encoded at a particular image location ($\boldsymbol{r_0}$). Equation 4 therefore correctly describes so-called "displacement artifacts" that occur in Fig. 1 when upstream dynamics is inevitably mapped to downstream image locations [13].

2.2. Statistical Dynamics & Foundations for CFD

Equation 4 forms the foundation for a general CFD approach that predicts apparent ^{3}He gas velocity from simulated airflow, measured gas diffusion, and known imaging conditions. It is noted, however, that predicted values are strictly a first order approximation. This is because higher order correlations generally contribute to the relative phase measured in PC-MRI [6,12]. Nevertheless, previous work shows that these are negligible in straight pipes with diameters typical for rat airways [6]. Possible impact is therefore not considered.

In previous PC-MRI studies of rat pulmonary airflow, ^{3}He gas was delivered during inhalation at a constant flow rate (~3.00 cc s^{-1}) [6]. In the trachea, where the typical diameter (d) is roughly 0.2 cm, the average gas velocity across the airway lumen ($\bar{v}$) is then ~95 cm s^{-1}. Given the kinematic viscosity (η/ρ) for ^{3}He gas at atmospheric pressure and typical body temperature (~37.5°C for a rat) is ~ 1.7 cm^2 s^{-1} [14], PC-MRI is conducted at a low Reynold's number ($Re = \bar{v}d\rho/\eta$ ~ 11). Since this is much lower than the transitional value to turbulence (~2100), laminar airflow is expected. Moreover, because the diffusion coefficient (D) for pure ^{3}He gas is ~ 1.85 cm^2 s^{-1} [15], gas transport is also characterized by a small Péclet number ($\bar{v}\,d/D$ < 11). Consequently, the combined effects of convection ($\bar{v}d$) and diffusion (D) are both expected to be important.

When convection-diffusion governs mass transport, and flow is steady, it is customary to describe each molecule's time-dependent location $\boldsymbol{r}(t)$ as a stationary Markov process [16]. It is also helpful to recognize that phase encoding and echo refocusing are both relatively short in Fig. 1, and as a consequence, it is reasonable to assume that spatial encoding is instantaneous at the center of each encoding event. In this case, $P(\boldsymbol{r}|\,\boldsymbol{r_0},\,\tau_j - t)d\boldsymbol{r}$ describes the conditional probability that a gas molecule initially within $d\boldsymbol{r}$ of $\boldsymbol{r}$ at time t will be at $\boldsymbol{r_0}$ when location is encoded at $t=\tau_j$ in Fig. 1. The ensemble average in Eq. 4 is then calculated as an integral over all possible starting locations within the flow domain Ω, such that –

$$\left\langle \boldsymbol{r}_j(t) \right\rangle = \int_{\Omega} \boldsymbol{r}_j P\left(\boldsymbol{r} \middle| \boldsymbol{r}_{\mathbf{o}}, \tau_j - t\right) d\boldsymbol{r}. \tag{5}$$

Substituting back into Eq. 4, and letting $t' = \tau_j - t$, then gives the following expression for apparent velocity –

$$\boldsymbol{v}_{app}^{j}(\boldsymbol{r}_{\mathbf{o}}) = \frac{1}{\delta \Delta G_j} \int_0^{\tau_i} R_j(\boldsymbol{r}_{\mathbf{o}}, t') G_j^*(t') dt'. \tag{6}$$

Here, the time origin is simply shifted to define the effective gradient waveform $\left(G_j^*\right)$ -

$$G_j^*(t') = G_j(\tau_j - t'), \tag{7}$$

and $R_j(\boldsymbol{r}_0, t')$ represents a "tracking field" that logs the average time-dependent coordinates for all molecules encoded at each image location $\boldsymbol{r}_0$ –

$$R_j(\boldsymbol{r}_{\mathbf{o}}, t') = \int_{\Omega} \boldsymbol{r}_j P(\boldsymbol{r} \middle| \boldsymbol{r}_{\mathbf{o}}, t') d\boldsymbol{r}. \tag{8}$$

Since the conditional probability density $P(\boldsymbol{r}|\boldsymbol{r}_0, t')$ obeys the convection-diffusion (i.e. forward Fokker-Planck) equation, it is known that [16] –

$$\frac{\partial P\left(\boldsymbol{r} \middle| \boldsymbol{r}_{\mathbf{o}}, t'\right)}{\partial t'} + \boldsymbol{V}(\boldsymbol{r}_{\mathbf{o}}) \bullet \nabla_{r_{\mathbf{o}}} P\left(\boldsymbol{r} \middle| \boldsymbol{r}_{\mathbf{o}}, t'\right) - D \nabla_{r_{\mathbf{o}}}^2 P\left(\boldsymbol{r} \middle| \boldsymbol{r}_{\mathbf{o}}, t'\right) = 0, \tag{9}$$

for $t' > 0$ and $\boldsymbol{r}_0 \in \Omega$. Here, $\boldsymbol{V}(\boldsymbol{r}_0)$ represents the CFD predicted airflow velocity at the image location $\boldsymbol{r}_0$, and D is the measured diffusion coefficient for ^{3}He gas. It is also known that for reflective boundary conditions [17] –

$$\nabla_{r_{\mathbf{o}}} P\left(\boldsymbol{r} \middle| \boldsymbol{r}_{\mathbf{o}}, t'\right) \bullet \boldsymbol{n}(\boldsymbol{r}_{\mathbf{o}}) = 0, \tag{10}$$

where $\boldsymbol{n}(\boldsymbol{r}_0)$ is the unit normal to any boundary at $\boldsymbol{r}_0$. In this case, the Appendix shows that each component of the tracking field (R_j) satisfies the convection-diffusion equation with reflective boundary conditions and an initial state defined by image coordinates (i.e. $R_j(\boldsymbol{r}_{\mathbf{o}}, 0) = \boldsymbol{r}_{\mathbf{o}}^j$). In practice, this is efficiently exploited by using the convection-diffusion equation and zero Neumann boundary conditions to independently evolve the tracking field (R_j) after it is first initialized with image coordinates. Evolution over encoding events in Fig. 1 then provides a basis for numerically evaluating Eq. 6 and predicting apparent gas velocity ($\boldsymbol{v}_{app}^j$) from simulated airflow patterns $\boldsymbol{V}(\boldsymbol{r}_0)$ and measured gas diffusion (D).

3. Materials and Methods

3.1. ^{3}He Gas Generation & Delivery

Previous methods have been described for producing two 110-ml vessels that are each pressurized with ~ 7.5 atmospheres of hyperpolarized ^{3}He gas [6,18]. Like previously, one vessel was used to acquire a high-resolution, 3D view of rat pulmonary airways, and the other for lower-resolution, 3D PC-MRI [6]. Prior to use, pure ^{3}He gas from a single vessel was released into a 2-liter Tedlar bag (Jensen Inert Products, Coral Springs, FL) where it was immediately diluted with N_2 to ensure sufficient gas volume.

Imaging was performed on a male Sprague-Dawley rat (Charles River Laboratories, Wilmington, MA) weighing ~267 grams. Prior to raw data collection, the rat was anesthetized with ~3% isoflurane in oxygen-enriched air (3:7 volume mixture of O_2 in N_2). It was then intubated using a 14-gauge catheter tube pre-cut to the proper length. After intubation, pulmonary gas flow was measured by attaching one end of a Fleisch 000 pneumotach (Emka Technologies, Paris, France) to the tracheal catheter, and the other to a homebuilt, computer-controlled ventilator that was previously described [19]. During ventilation the pressure differential across the pneumotach was monitored using a commercial transducer (TRD5100, Buxco Electronics, Troy, NY) whose signal was amplified and displayed on a digital oscilloscope. Prior to use, the transducer was calibrated using standard methods [20]. Measured voltage registered on the oscilloscope could then be read directly as volumetric flow (cc s^{-1}), and temporal integration provided direct estimates for inhaled gas volume.

Like in prior work, two 0.8-second-long breathing cycles were continuously repeated [6]. For ventilator setup, drive pressures were adjusted so the first cycle administered ~3.5 ml of oxygen-enriched air (with ~3% isoflurane) over a 320 ms inhalation that was then followed by a 480 ms exhale. The second cycle then delivered ~0.7 ml of gas out of the Tedlar bag during its first 240 ms [6]. This was immediately followed by a push of pure oxygen that lasted 296 ms and was delivered at the same inhalation rate (i.e. ~0.7cc/0.24 s ~ 2.9 cc s^{-1}) [6]. To trigger MRI data acquisition during this part of the breathing cycle, the ventilator generated a TTL pulse 25 ms after the start of each oxygen push. The last 264 ms of the 2nd cycle was then used for exhale.

After setting ventilator drive pressures to achieve specified flows, the pneumotach was removed so the tracheal tube could be attached directly to the ventilator during imaging. Generally, this was necessary because the pneumotach completely depolarized ^{3}He gas. It was also observed that delivered gas flow was sensitive to the entry angle and insertion depth of the tracheal catheter. Since the ventilator is pressure controlled, this suggests that precise catheter orientation (and possibly the amount of phlegm near the tip) significantly mediates system backpressure. Consequently, initial flow rates set with the pneumotach merely served as a guide and were not strictly maintained when it was detached for imaging.

3.2. PC-MRI

All MRI was performed at 2.0T and previous work describes all hardware, raw data collection, and image reconstruction [19]. In the current study 3D PC-MRI was performed using motion-encoding gradients (G_j) of 4, 4, and 3 Gauss cm^{-1} along x, y, and z respectively. Like previously [6,19], radial sampling employed 128 different projections that were each collected using 128 complex time-domain points, a field-of-view (FOV) of 6.4 cm, and a 51 kHz bandwidth. Phase encoding along the z-axis employed 32 steps and the same FOV. After raw data collection, radial data was regridded onto a Cartesian 128×128×32 matrix, and 3D images were Fourier reconstructed with a sampling resolution of ~ 0.5×0.5×2 mm [19].

During mechanical ventilation each TTL pulse triggered 32 phase-encoded projections that were acquired using an 8 ms repetition time (TR) over 256 ms of constant inhaled gas flow. Raw data for each 3D image therefore took 128 breaths consuming ~ 90 ml (i.e. ~128*0.7) of total gas from the Tedlar bag. Since 1 trigger occurred every 1.6 seconds, each 3D data set required ~ 3.4 minutes to collect. Total time for PC-MRI was therefore about 14 minutes. Although the T_1 for ^{3}He in the bag was over 30 minutes [19], data acquisition was interleaved so T_1-losses would be the same for all PC-MRI data. This was achieved by – 1) acquiring phase-encoded data with different motion-encoding over four consecutive breaths,

2) incrementing the projection angle, and 3) repeating to accumulate all remaining data [6,19].

After Fourier reconstruction all PC-MRI results were processed in *Mathematica*™ using Eq. 1. Velocity values were then compiled into (legacy) VTK file format (http://www.vtk.org/) for rendering and analysis in *ParaView* – an open-source visualization environment (http://www.paraview.org/). Estimated uncertainty for each velocity component (j) was also compiled for integrated display and analysis. At each pixel this was calculated as the predicted standard deviation (δ_v^j) using the signal-to-noise ratio (SNR) and known motion sensitivity (α_j) [21] –

$$\delta_v^j = \pi \Big/ \left(SNR_j \, \alpha_j \right) . \tag{11}$$

Here, values for SNR are derived using the localized PC-MRI signal strength and the magnitude of average noise.

3.3. High-Resolution ^{3}He MRI

To more accurately capture airway structure for CFD, PC-MRI was supplemented with higher-resolution ^{3}He images acquired using a pulse sequence similar to that in Fig. 1. This utilized the second vessel of hyperpolarized ^{3}He gas, had no motion encoding, and increased spatial resolution by employing 200 projections and 128 phase encoding steps. All other acquisition parameters were the same except that the oxygen push was decreased slightly to reduce possible image blurring. Re-gridding of planar radial data was also onto a 256×256 matrix rather than the 128×128 used for PC-MRI. Sampling resolution was then 0.25×0.25×0.5 mm along x, y, and z respectively [19]. To achieve isotropic volume elements of 0.25 mm, zero filling was employed along the phase-encode axis prior to Fourier reconstruction.

3.4. CFD

High-resolution ^{3}He images were segmented using a 3D connected threshold with subsequent surface mesh generation [22]. The surface mesh was then smoothed using a volume-conserving algorithm that was previously described [23]. To help impose boundary conditions for CFD, terminal airways in the smoothed surface mesh were automatically chopped to create well-defined outlets perpendicular to the lung's medial axis [24]. A tetrahedral volume mesh was then generated using in-house code that automatically varies the size of mesh elements to match the scale of local airway features [25]. For efficient CFD using a lower number of mesh elements, a "honeycomb" polyhedral mesh dual to the tetrahedral volume mesh was created using the polyDualMesh utility in OpenFOAM (OpenCFD Ltd, Reading, UK). Simulated airflow was then predicted in OpenFOAM by solving the laminar, 3D, incompressible Navier-Stokes equations for fluid mass and momentum on the polyhedral mesh. To formulate a steady state solution, no-slip boundary conditions were employed at all airway walls, inlet pressure at the trachea was arbitrarily set to zero, and PC-MRI results were used to specify airflow (cc s^{-1}) at the trachea and all terminal outlets.

Once local airflow patterns (i.e. $\boldsymbol{V}(\boldsymbol{r_0})$) were predicted, results were employed to compute apparent velocity values ($\boldsymbol{v}_{app}^j$) according to Eq. 6. This first required predicting the tracking field $R_j(\boldsymbol{r_0}, t')$– which has already been shown to satisfy the convection-diffusion equation with zero-Neumann boundary conditions. Specific solutions were formulated in OpenFOAM after initializing starting values with imaging coordinates, such that -

$R_j(\boldsymbol{r}_o, 0) = \boldsymbol{r}_o^j$. Generally, this is dictated by Eq. 8 and the fact that $P(\boldsymbol{r}|\boldsymbol{r_0}, t'=0)$ is, by definition, the Dirac delta function.

After initializing the tracking field at $t'=0$, starting values were evolved in time using the convection-diffusion equation and discrete time steps dt' (1 μs). The integral in Eq. 6 was then approximated using the sum of $R_j(\boldsymbol{r}_o, t')\, G_j^*(t')\, dt' / \left(\delta \Delta G_j\right)$. In Fig. 1 $G_j^*(t')/G_j$ is just 1, 0, or −1. It can therefore be seen that $\boldsymbol{v}_{app}^j$ in Eq. 6 is simply the time-averaged value of the tracking field $R_j(\boldsymbol{r_0}, t')$ during the second gradient pulse minus the average during the first – all divided by their separation time (Δ). Of course, actual gradient pulses have a finite rise-time that could potentially influence numerical integration. In the current study, however, the measured rise-time (~60 μs) was much shorter than either the gradient pulse duration (δ) or separation time (Δ). Possible effects are therefore expected to be small and are ignored.

4. Results

4.1. CFD Benchmarking

Numerical methods for predicting apparent velocity were benchmarked against analytical solutions formulated for laminar gas flow at 1.0 cc s^{-1} through a straight tube with a 0.3 cm diameter. Gas was assumed to be a binary mixture of ^{3}He in N_2 with a mole fraction of 0.4 for ^{3}He. In this case the ^{3}He diffusion coefficient (D) is expected to be ~ 1.0 ($cm^2\ s^{-1}$) [15] and the dynamic viscosity is ~ 186.6×10^{-6} Poise ($g\ cm^{-1}\ s^{-1}$) [26].

Figure 2 shows that CFD and analytical solutions to the Navier-Stokes equations are identical for laminar airflow in a straight tube. In both cases, predicted flow is directed down the tube's symmetry (z) axis and local velocity ($\boldsymbol{V}_z$) exhibits a familiar radial profile. Results also show that CFD and analytical predictions for apparent velocity ($\boldsymbol{v}_{app}^z$) are the same. Like the actual velocity ($\boldsymbol{V}_z$), apparent values also display radial symmetry. The apparent profile is, however, different – being lower at the tube's center and higher at its wall. Physically, this is the direct result of gas diffusion across multiple streamlines during different encoding events in Fig. 1. The end result is that PC-MRI measures a blurred flow structure ($\boldsymbol{v}_{app}^z$) that does not strictly reflect the actual flow domain ($\boldsymbol{V}_z$) but rather its spatial and temporal average (dictated through Eq. 6).

In directions transverse to the tube's symmetry axis, solutions to the Navier-Stokes equations predict zero velocity (i.e. $\boldsymbol{V}_x = \boldsymbol{V}_y = 0$). Nevertheless, molecular diffusion still occurs, and Fig. 3 shows that associated Brownian displacements give rise to finite apparent velocity in off-axis directions (i.e. $\boldsymbol{v}_{app}^x$ and $\boldsymbol{v}_{app}^y$). If one were to imagine their vector sum, results in Fig. 3 would exhibit a radial profile that is zero at the tube's center and points outward with increasing amplitude near tube walls. The outward orientation of their vector sum therefore makes it appear as if there is a net outward flow that radiates from the tube's center in off-axis directions. Since these results are identical whether predicted using either analytical or CFD methods, their equivalence is confirmed. The peculiar behavior, however, warrants brief explanation since it was not previously discussed [6,10].

To understand apparent flow in Fig. 3 it is helpful to first recognize that motion is encoded before position in Fig. 1. If gas location is therefore encoded at the tube wall, it is statistically likely that molecules encoded at that position must have diffused from some interior point. This is different for gas position encoded at the tube's center, since there it is equally likely to have diffused from any direction. Averaging over all possibilities then gives zero for apparent velocity at the tube's center. More generally, as encoded location in

the transverse plane moves off center towards the tube wall it becomes more and more likely that gas had initially diffused from an interior location, thereby resulting in larger and larger values of apparent outward velocity. Of course, the precise behavior depends on the gas diffusion rate and encoding times. Both therefore mediate the precise flow structure predicted in Fig. 3.

Despite the anomalous structure of apparent gas velocity in a narrow tube, volumetric flow is conserved. This was tested in *ParaView* by selecting arbitrary slices at different oblique angles across CFD results. Flow was then calculated by integrating the vector dot product between apparent velocity ($\boldsymbol{v}_{app}$) and the normal for each slice. In all cases the same flow rate used for CFD (1 ± 0.01 cc s^{-1}) was obtained. This generalizes previous analytical results where gas flow measured with PC-MRI was shown to be correct in straight narrow tubes, specifically, when calculated using only axial velocity [6]. Here, a more general result for oblique slices is obtained simply by exploiting a full 3D formulation of the same problem.

4.2. MRI Data and CFD Input

Figure 4A shows high-resolution ^{3}He imaging results, and Fig. 4B highlights segmented airways after a global threshold is applied to retain only those regions where the SNR is greater than 20. Segmentation is seen to effectively isolate conducting airways; specifically, by eliminating weaker MRI signal from surrounding parenchyma. By comparison, architectural detail in PC-MRI is generally less evident due to its lower spatial resolution (and deeper gas penetration since the O_2 push was not reduced). This is illustrated in Fig. 4C where segmented airways are overlaid with measured values for inhaled gas speed. Structural differences are especially apparent along the z-axis where coarse PC-MRI resolution is comparable to smaller airway dimensions. This is particularly challenging for defining inlet and outlet flows for CFD since uncertainty in structural boundaries can adversely affect the accuracy of flow measurements performed with PC-MRI [27]. To minimize this as much as possible, linear interpolation was employed to re-sample measured gas dynamics onto segmented airways. This was performed in *ParaView* using its '*ResampleWithDataset*' filter, and results in Fig. 4D highlight resulting integration of measured structure and dynamics. Also shown in Fig. 4E is a colorized map identifying different airways that were used to measure regional airflow for CFD boundary conditions.

Table 1 summarizes regional airflow measurements performed using MRI data shown in Fig. 4D. Results generally reflect the varying severity of partial volume effects that occur when resolved volume elements in PC-MRI are large enough to contain substantially different flow velocities [28]. This is particularly problematic for accurately measuring flow to each lung lobe where small airway size and close proximity to the surrounding parenchyma means that measured phase often reflects the complex sum of MRI signal from both gas-filled regions. Since Fig. 4C shows that gas in the parenchyma is more-or-less stationary, this partial volume effect artificially slows measured gas velocity [28]. This likely explains why the total airflow calculated by summing individual flows to all lung lobes (1.68 ± 0.10 cc s^{-1}) is significantly lower than the measured flow in the upper trachea (2.58 ± 0.08 cc s^{-1}). Table 1 also shows that cross-sectional area is often substantially lower in distal airways. This is important because – 1) segmented structures derived from a threshold are preferentially eroded as their actual size decreases relative to image resolution [29], and 2) this makes PC-MRI flow measurements in narrow structures even more susceptible to underestimation [28].

Partial volume effects also influence measured airflow in the transition zone (2.25 ± 0.13 cc s^{-1}) where the tracheal lumen rapidly broadens before splitting into right and left bronchi. In Fig. 4 it is seen that this broadening occurs on a length-scale comparable with the z-

resolution of PC-MRI data. Rapid changes in airway lumen therefore mean that different gas velocities ultimately contribute to local PC-MRI results. Curvature away from the z-axis (not shown) also means that resolved volume elements contain different streamlines as inhaled airflow is directed into the deep lung. This in contrast with the upper trachea where the airway lumen is relatively constant, orientation is well aligned with the z-axis, and MRI signal from the parenchyma is not mixed in.

In light of above results it is clear that no single inhaled flow rate characterizes all PC-MRI data. Since the mean airflow in the trachea, transition zone, and airways feeding each of the lung's 5 lobes is ~2.0 (cc s^{-1}) - this value was used for CFD. Measurements of ^{3}He gas diffusion at the center of larger airways could also be derived using PC-MRI data [19], and since the typical value (~ 1.0 cm^2 s^{-1}) is expected for a binary mixture of ^{3}He in N_2 when the ^{3}He mole fraction is ~0.4 [15], this composition was assumed for pulmonary CFD. The same dynamic viscosity already used for benchmarking numerical predictions in straight tubes was therefore employed.

In addition to specifying inhaled airflow at the trachea, CFD also required airflows at all terminal outlets. Since partial-volume effects and uncertainty in actual airway boundaries prevented accurate measurement with PC-MRI, required values were estimated by first determining the fraction of inhaled airflow going to each lung lobe. This was calculated from Table 1 simply by dividing the measured flow to each lobe by the lobar total (1.68 ± 0.10 cc s^{-1}). Now, for any specified airflow at the trachea (i.e. 2 cc s^{-1}), the total flow feeding each lung lobe could be estimated by multiplying the tracheal airflow by the lobar fraction. The airflow at any outlet within a lobe was then set to the expected lobar flow and weighted by the ratio of that outlet's cross-sectional area to the total area for all outlets within the same lobe. This generally accounts for measured flow splits and utilizes simple scaling that is commonly employed to partition flow in branched airway models [30].

4.3. MRI and CFD Comparisons

Fig. 5A shows predicted gas velocity along the z-axis when CFD is used to solve the Navier-Stokes equations for $\boldsymbol{V}_z$ in rat pulmonary airways. Due to the low Reynold's number, results exhibit laminar flow patterns that are characterized by zero gas velocity along airway walls and higher values at airway centers. This is less evident in Fig. 5B where predicted values for apparent velocity ($\boldsymbol{v}_{app}^{z}$) are shown. In the trachea, diffusion across different laminar flow streams is seen to reduce apparent velocity at the airway center and increases it near the wall – just like in straight tubes [6,10]. As pulmonary airways become less aligned with the z-axis restricted diffusion then introduces anomalous flow structure that appears along different airway edges where free gas diffusion along the z-axis is impeded by airway walls.

Measured values for apparent ^{3}He velocity along the z-axis ($\boldsymbol{v}_{app}^{z}$) are shown in Fig. 5C. Although qualitatively similar to Fig. 5B, local velocity is clearly different depending on location. In principle, this is due to the fact that CFD was performed using the average flow rate from PC-MRI measurements in different airway regions. In the upper trachea, where partial volume effects and segmentation errors are both relatively minor, this means that measured airflow in PC-MRI is higher than the average used for CFD. In Figs. 5B&C this is accurately reflected by obvious tracheal differences between predicted and measured velocity. Similar rationale also explains differences in the deeper lung where more significant partial-volume effects mean that measured airflow is lower than the average used for CFD and, as a consequence, predicted values for apparent z-velocity are somewhat higher than measured. Fig. 6A shows these regional differences more quantitatively in a correlation plot. There, higher PC-MRI values in the trachea fall below a perfect correlation; whereas, lower values in the deeper lung fall above. Despite these differences, however,

overall correlation throughout pulmonary airways is reasonably good ($R^2 = 0.68$). By comparison, Fig. 6B shows that correlations are substantially worse ($R^2 = 0.37$) if apparent transport is ignored and PC-MRI is simply compared with straight CFD (i.e. $\boldsymbol{V}_z$).

Figure 7A shows predicted gas velocity along the x-axis when CFD is used to solve the Navier-Stokes equations for $\boldsymbol{V}_x$. In most airways velocity is much slower than along the z-axis. In the trachea, for example, $\boldsymbol{V}_x$ is nearly zero. Figure 7B however, predicts substantial values for apparent velocity ($\boldsymbol{v}_{app}^{x}$). Generally, these are dominated by restricted diffusion since actual flow velocity (i.e. $\boldsymbol{V}_x$) is slow. Under these conditions apparent velocity patterns in the trachea are nearly identical to those in straight tubes (see Fig. 3). As gas moves deeper into pulmonary airways the same patterns are repeated but appear roughly superimposed with larger local velocity values (i.e. $\boldsymbol{V}_x$). Figure 7C shows very similar patterns in PC-MRI, and in Fig. 6C regression analysis shows good correlation ($R^2 = 0.87$) between measured and predicted values of apparent velocity ($\boldsymbol{v}_{app}^{x}$). Like z-values, however, correlations are relatively poor ($R^2 = 0.20$) if apparent transport is ignored and straight CFD (i.e. $\boldsymbol{V}_x$) is simply compared with PC-MRI (Fig. 6D).

Overall, x- and y-velocity components behave similarly. Like $\boldsymbol{V}_x$, Fig. 8A shows that actual gas velocity along the y-axis ($\boldsymbol{V}_y$) is relatively slow. Consequently, predicted values for apparent velocity ($\boldsymbol{v}_{app}^{y}$) are again dominated by restricted diffusion (Fig. 8B). Predicted patterns of apparent velocity along the y-axis also agree well with PC-MRI (Fig. 8C), and linear regression gives comparable correlations (Fig. 6E / $R^2 = 0.83$) that are again relatively poor if apparent transport is ignored (Fig. 6F / $R^2 = 0.14$).

4.4. Predicted Effects of Apparent Transport on Pulmonary Airflow Measurements

Unlike actual PC-MRI data, CFD is unencumbered by either partial volume effects or segmentation errors. Simulation results therefore provide a unique opportunity for examining how apparent transport potentially impacts pulmonary airflow measurements if based on idealized PC-MRI data. Assuming actual airflow is defined by straight CFD results (i.e. $\boldsymbol{V}$), Table 2 summarizes the percentage of actual airflow measured from numerical predictions of apparent ^{3}He velocity ($\boldsymbol{v}_{app}$). In the trachea and left bronchi, where airway structure is similar to a straight tube, airflow is seen to be fairly accurate when measured from numerical predictions of apparent transport. In smaller pulmonary airways, however, measured airflow exhibits a distinct upward bias. Values are also highly variable with the largest flows being measured nearest the parent airway. In the right upper (RU) branch, for example, Figs. 7B&C show that restricted diffusion causes anomalous velocity in the trachea near the entrance into the RU branch. Measured flow in the vicinity is therefore enhanced by anomalous values that point directly into the RU lobe. The same occurs near the right middle and accessory branches where Figs. 8B&C show significant y-contributions. Of course, in-vivo flow measurements are also susceptible to partial-volume effects. Reduced flow in Table 1 therefore indicates that these generally override the upward bias predicted from apparent transport alone. As a whole, this suggests that the best approach to measure lobar flow from actual in-vivo PC-MRI data is nearest to the lobe's parent airway, particularly since enhanced flow from apparent transport then partially compensates reductions from partial volume effects. This overall strategy was therefore employed for measurements summarized in Table 1.

5. Discussion

Results in Fig. 6 show that correlations between predicted values of apparent velocity and PC-MRI are better in the xy-plane than along the z-axis. This is likely due to the fact that transport along z is more impacted by flow. This is important since flow velocity scales

roughly with the square of airway diameter [30], whereas it can be shown that apparent velocity at the airway wall is independent of airway size when restricted diffusion dominates. Small errors in airway geometry specified for CFD therefore introduce more variance in apparent z-velocities than xy-counterparts.

Based on the above arguments it is not surprising that scatter for x- and y-correlations (Figs. 6C & E) falls largely within predicted standard deviations based on estimated PC-MRI measurement uncertainty (i.e. Eq. 11). The only other trend from linear regression is a slightly steeper slope – which is consistent with expected partial volume effects since coarse PC-MRI resolution inevitably slows measured velocity. A similar trend is observed for z-components in Fig. 6A. In this case, however, higher sensitivity to flow and associated segmentation errors makes variations fall outside those simply predicted from PC-MRI measurement uncertainty alone.

Although apparent ^{3}He gas velocity is accurately predicted by CFD it is unclear if inverse methods can be applied to recover actual airflow patterns from PC-MRI. Current use for assessing patient-specific airflow models is therefore indirect, whereby, CFD must be used to predict PC-MRI results. While still useful, this inevitably limits model testing since diffusion-mediated effects reduce laminar detail and introduce anomalous structure that can obscure slow flow. Since diluting ^{3}He with a heavier gas like C_3F_8 significantly decreases ^{3}He diffusion rates (from ~ 1.0 in the current study to ~0.36 $cm^2\ s^{-1}$), and this has already been found to increase laminar detail in PC-MRI [6], higher-fidelity CFD testing is feasible. It can also be shown that anomalous velocity at airway walls scales with $\sqrt{D}$ - so diluting ^{3}He with heavier gas also likely improves model assessments in slow airflow regions.

Like quick gas diffusion, lengthy delays between PC-MRI encoding events can exaggerate apparent transport. One common approach to minimize this is to place any phase-encoding between the alternating gradient pulses used for encoding motion [13]. In aerodynamic studies with a heavier (less MRI sensitive) gas this approach is so affective that the idea of apparent transport is unnecessary and good agreement between PC-MRI and straight CFD (i.e. $\boldsymbol{V}$) is observed simply by employing pure phase encoding together with superimposed motion encoding [31]. While impractical for 3D in-vivo imaging due to excessively long acquisition times, these results demonstrate how coincident encoding and more favorable gas composition can be combined to dramatically reduce apparent transport and facilitate higher-fidelity CFD testing.

Results from this study clearly indicate that improved imaging resolution would be beneficial for future CFD assessments in small laboratory animals. It would therefore be beneficial to employ variable RF flip angles since this improves the SNR in ^{3}He MRI and reduces artifacts for higher-resolution imaging [32]. Compressed sensing also reduces required spatial encoding [33], and this allows for improved SNR and resolution in PC-MRI [34]. By exploiting both it seems feasible to at least double z-resolution in the current study without significant loss in either SNR or measurement accuracy. Of course, higher resolution might be achievable but then precise trade-offs in SNR and flow accuracy need to be more carefully examined [34].

Finally, it is important to consider recent in-vitro work where ^{3}He PC-MRI was successfully employed to assess CFD predictions in a human-size model of proximal airways [35]. In that study, good agreement between straight CFD (i.e. $\boldsymbol{V}$) and ^{3}He PC-MRI was observed even though apparent transport wasn't considered. This agreement, however, was primarily limited to axial velocity in regions dominated by high airflow. By comparison, significant differences were reported near airway walls and in off-axis directions [35], precisely where

molecular diffusion and apparent transport is expected to be more important. Correlations between measured and predicted gas velocity were also reduced in high shear regions [35] where conditions are more similar to rat airways, and laminar blurring occurs due to rapid gas diffusion across neighboring flow streams. These observations suggest that apparent transport is not only important for improving CFD assessments in rats but also at the human scale.

6. Conclusions

Results from this study show that ^{3}He PC-MRI provides apparent values of local gas velocity that are accurately predicted using CFD, measured gas diffusion, and information about PC-MRI encoding. In rat pulmonary airways, apparent velocity measured with ^{3}He PC-MRI reduces laminar detail and introduces anomalous flow structure that reflects restricted gas diffusion at airway walls. Since such anomalous structure can also obscure slow flow, apparent transport generally reduces the testable detail that ^{3}He PC-MRI can capture for quantitative comparisons with patient-specific airflow predictions. Partial volume effects also complicate PC-MRI data and, as a result, future improvements aimed at higher-fidelity CFD testing should not only reduce the severity of apparent transport but also increase achievable image resolution.

Acknowledgments

Research was performed in the Environmental Molecular Sciences Laboratory (a national scientific user facility sponsored by the US Department of Energy's Office of Biological and Environmental Research) located at Pacific Northwest National Laboratory (PNNL), and operated for DOE by Battelle. Special thanks to Angie Woodstock (PNNL) for animal handling and financial support provided by NIH NHLBI RO1 HL073598.

Appendix

Mathematical proof exploits the commutation of the convection-diffusion operator -

$$\begin{aligned}\left(\frac{\partial}{\partial t'}+\boldsymbol{V}(\boldsymbol{r}_o)\bullet\nabla_{\boldsymbol{r}_o}-D\nabla^2_{\boldsymbol{r}_o}\right)R_j(\boldsymbol{r}_o,t')&\\ =\left(\frac{\partial}{\partial t'}+\boldsymbol{V}(\boldsymbol{r}_o)\bullet\nabla_{\boldsymbol{r}_o}-D\nabla^2_{\boldsymbol{r}_o}\right)\int_\Omega \boldsymbol{r}_j P\left(\boldsymbol{r}\middle|\boldsymbol{r}_o,t'\right)d\boldsymbol{r}&\\ =\int_\Omega \boldsymbol{r}_j\left(\frac{\partial P\left(\boldsymbol{r}\middle|\boldsymbol{r}_o,t'\right)}{\partial t'}+\boldsymbol{V}(\boldsymbol{r}_o)\bullet\nabla_{\boldsymbol{r}_o}P\left(\boldsymbol{r}\middle|\boldsymbol{r}_o,t'\right)-D\nabla^2_{\boldsymbol{r}_o}P\left(\boldsymbol{r}\middle|\boldsymbol{r}_o,t'\right)\right)d\boldsymbol{r}=0,&\end{aligned} \tag{A1}$$

and similarly

$$\nabla_{\boldsymbol{r}_o}R_j(\boldsymbol{r}_o,t')\bullet\boldsymbol{n}(\boldsymbol{r}_o)=\left(\nabla_{\boldsymbol{r}_o}\int_\Omega \boldsymbol{r}_j P\left(\boldsymbol{r}\middle|\boldsymbol{r}_o,t'\right)d\boldsymbol{r}\right)\bullet\boldsymbol{n}(\boldsymbol{r}_o)=\int_\Omega \boldsymbol{r}_j\left(\nabla_{\boldsymbol{r}_o}P\left(\boldsymbol{r}\middle|\boldsymbol{r}_o,t'\right)\bullet\boldsymbol{n}(\boldsymbol{r}_o)\right)d\boldsymbol{r}=0 \tag{A2}$$

References

1. Longest PW, Holbrook LT. In silico models of aerosol delivery to the respiratory tract - Development and applications. Adv Drug Deliv Rev. 2011
2. Kleinstreuer C, Zhang Z, Kim CS. Effects of curved inlet tubes on air flow and particle deposition in bifurcating lung models. J Biomech. 2001; 34:659–669. [PubMed: 11311707]
3. Tawhai MH, Hoffman EA, Lin CL. The lung physiome: merging imaging-based measures with predictive computational models. Wires Syst Biol Med. 2009; 1:61–72.

4. Minard KR, Einstein DR, Jacob RE, Kabilan S, Kuprat AP, Timchalk CA, Trease LL, Corley RA. Application of magnetic resonance (MR) imaging for the development and validation of computational fluid dynamic (CFD) models of the rat respiratory system. Inhal Toxicol. 2006; 18:787–794. [PubMed: 16774868]
5. Oldham MJ. Challenges in validating CFD-Derived inhaled aerosol deposition predictions. Inhal Toxicol. 2006; 18:781–786. [PubMed: 16774867]
6. Minard KR, Jacob RE, Laicher G, Einstein DR, Kuprat AP, Corley RA. MR imaging of apparent He-3 gas transport in narrow pipes and rodent airways. Journal of Magnetic Resonance. 2008; 194:182–191. [PubMed: 18667344]
7. de Rochefort L, Maitre X, Fodil R, Vial L, Louis B, Isabey D, Croce C, Darrasse L, Apiou G, Caillibotte G, Bittoun J, Durand E. Phase-contrast velocimetry with hyperpolarized He-3 for in vitro and in vivo characterization of airflow. Magn Reson Med. 2006; 55:1318–1325. [PubMed: 16700024]
8. Schroeter JD, Kimbell JS, Gross EA, Willson GA, Dorman DC, Tan YM, Clewell HJ. Application of physiological computational fluid dynamics models to predict interspecies nasal dosimetry of inhaled acrolein. Inhal Toxicol. 2008; 20:227–243. [PubMed: 18300045]
9. Pope JM, Yao S. Quantitative NMR imaging of flow. Concepts in Magnetic Resonance. 1993; 5:281–302.
10. Kaiser LG, Logan JW, Meersmann T, Pines A. Dynamic NMR microscopy of gas phase Poiseuille flow. Journal of Magnetic Resonance. 2001; 149:144–148.
11. Bush ML, Frederick CB, Kimbell JS, Ultman JS. A CFD-PBPK hybrid model for simulating gas and vapor uptake in the rat nose. Toxicol Appl Pharmacol. 1998; 150:133–145. [PubMed: 9630462]
12. Stepisnik J. Validity limits of Gaussian approximation in cumulant expansion for diffusion attenuation of spin echo. Physica B. 1999; 270:110–117.
13. Thunberg P, Wigstrom L, Ebbers T, Karlsson M. Correction for displacement artifacts in 3D phase contrast imaging. J Magn Reson Imaging. 2002; 16:591–597. [PubMed: 12412037]
14. Turner MJ, MacLeod IM, Rothberg AD. Effects of temperature and composition on the viscosity of respiratory gases. J Appl Physiol. 1989; 67:472–477. [PubMed: 2503494]
15. Acosta RH, Agulles-Pedros L, Komin S, Sebastiani D, Spiess HW, Blumler P. Diffusion in binary gas mixtures studied by NMR of hyperpolarized gases and molecular dynamics simulations. Phys Chem Chem Phys. 2006; 8:4182–4188. [PubMed: 16971986]
16. Arnold, L. Stochastic Differential Equations: Theory and Applications. New York: John Wiley & Sons; 1974.
17. Szymczak P, Ladd AJC. Boundary conditions for stochastic solutions of the convection-diffusion equation. Phys Rev E. 2003; 68
18. Jacob RE, Minard KR, Laicher G, Timchalk C. 3D He-3 diffusion MRI as a local in vivo morphometric tool to evaluate emphysematous rat lungs. J Appl Physiol. 2008; 105:1291–1300. [PubMed: 18719237]
19. Jacob RE, Laicher G, Minard KR. 3D MRI of non-Gaussian He-3 gas diffusion in the rat lung. Journal of Magnetic Resonance. 2007; 188:357–366. [PubMed: 17827044]
20. Minard KR, Wind RA, Phelps RL. A compact respiratory-triggering device for routine microimaging of laboratory mice. J Magn Reson Imaging. 1998; 8:1343–1348. [PubMed: 9848750]
21. Lotz J, Meier C, Leppert A, Galanski M. Cardiovascular flow measurement with phase-contrast MR imaging: basic facts and implementation. Radiographics. 2002; 22:651–671. [PubMed: 12006694]
22. Carson JP, Einstein DR, Minard KR, Fanucchi MV, Wallis CD, Corley RA. High resolution lung airway cast segmentation with proper topology suitable for computational fluid dynamic simulations. Comput Med Imaging Graph. 2010; 34:572–578. [PubMed: 20382502]
23. Kuprat A, Khamayseh A, George D, Larkey L. Volume conserving smoothing for piecewise linear curves, surfaces, and triple lines. Journal of Computational Physics. 2001; 172:99–118.

24. Jiao X, Einstein DR, Dyedov V, Carson JP. Automatic identification and truncation of boundary outlets in complex imaging-derived biomedical geometries. Med Biol Eng Comput. 2009; 47:989–999. [PubMed: 19526263]
25. Kuprat AP, Einstein DR. An anisotropic scale-invariant unstructured mesh generator suitable for volumetric imaging data. J Comput Phys. 2009; 228:619–640. [PubMed: 19784397]
26. Brokaw, RS. Viscosity of Gas Mixtures, NASA Technical Note D-4496. 1968.
27. Hoogeveen RM, Bakker CJ, Viergever MA. MR phase-contrast flow measurement with limited spatial resolution in small vessels: value of model-based image analysis. Magn Reson Med. 1999; 41:520–528. [PubMed: 10204875]
28. Tang C, Blatter DD, Parker DL. Accuracy of phase-contrast flow measurements in the presence of partial-volume effects. J Magn Reson Imaging. 1993; 3:377–385. [PubMed: 8448400]
29. Dame Carroll JR, Chandra A, Jones AS, Berend N, Magnussen JS, King GG. Airway dimensions measured from micro-computed tomography and high-resolution computed tomography. Eur Respir J. 2006; 28:712–720. [PubMed: 16870669]
30. Phillips CG, Kaye SR. On the asymmetry of bifurcations in the bronchial tree. Respir Physiol. 1997; 107:85–98. [PubMed: 9089897]
31. Newling B, Poirier CC, Zhi Y, Rioux JA, Coristine AJ, Roach D, Balcom BJ. Velocity imaging of highly turbulent gas flow. Phys Rev Lett. 2004; 93
32. Johnson GA, Cofer GP, Hedlund LW, Maronpot RR, Suddarth SA. Registered (1)H and (3)He magnetic resonance microscopy of the lung. Magn Reson Med. 2001; 45:365–370. [PubMed: 11241691]
33. Ajraoui S, Lee KJ, Deppe MH, Parnell SR, Parra-Robles J, Wild JM. Compressed sensing in hyperpolarized 3He lung MRI. Magn Reson Med. 2010; 63:1059–1069. [PubMed: 20373407]
34. Holland DJ, Malioutov DM, Blake A, Sederman AJ, Gladden LF. Reducing data acquisition times in phase-encoded velocity imaging using compressed sensing. Journal of Magnetic Resonance. 2010; 203:236–246. [PubMed: 20138789]
35. de Rochefort L, Vial L, Fodil R, Maitre X, Louis B, Isabey D, Caillibotte G, Thiriet M, Bittoun J, Durand E, Sbirlea-Apiou G. In vitro validation of computational fluid dynamic simulation in human proximal airways with hyperpolarized 3He magnetic resonance phase-contrast velocimetry. J Appl Physiol. 2007; 102:2012–2023. [PubMed: 17289906]

- ^{3}He MRI and CFD are complimentary tools for studying inhaled gas dynamics
- PC-MRI provides apparent values of ^{3}He gas velocity
- Depend on both airflow and gas diffusion
- Can be used to develop and test patient-specific CFD models of gas transport
- Accurately predict PC-MRI results in pulmonary airways

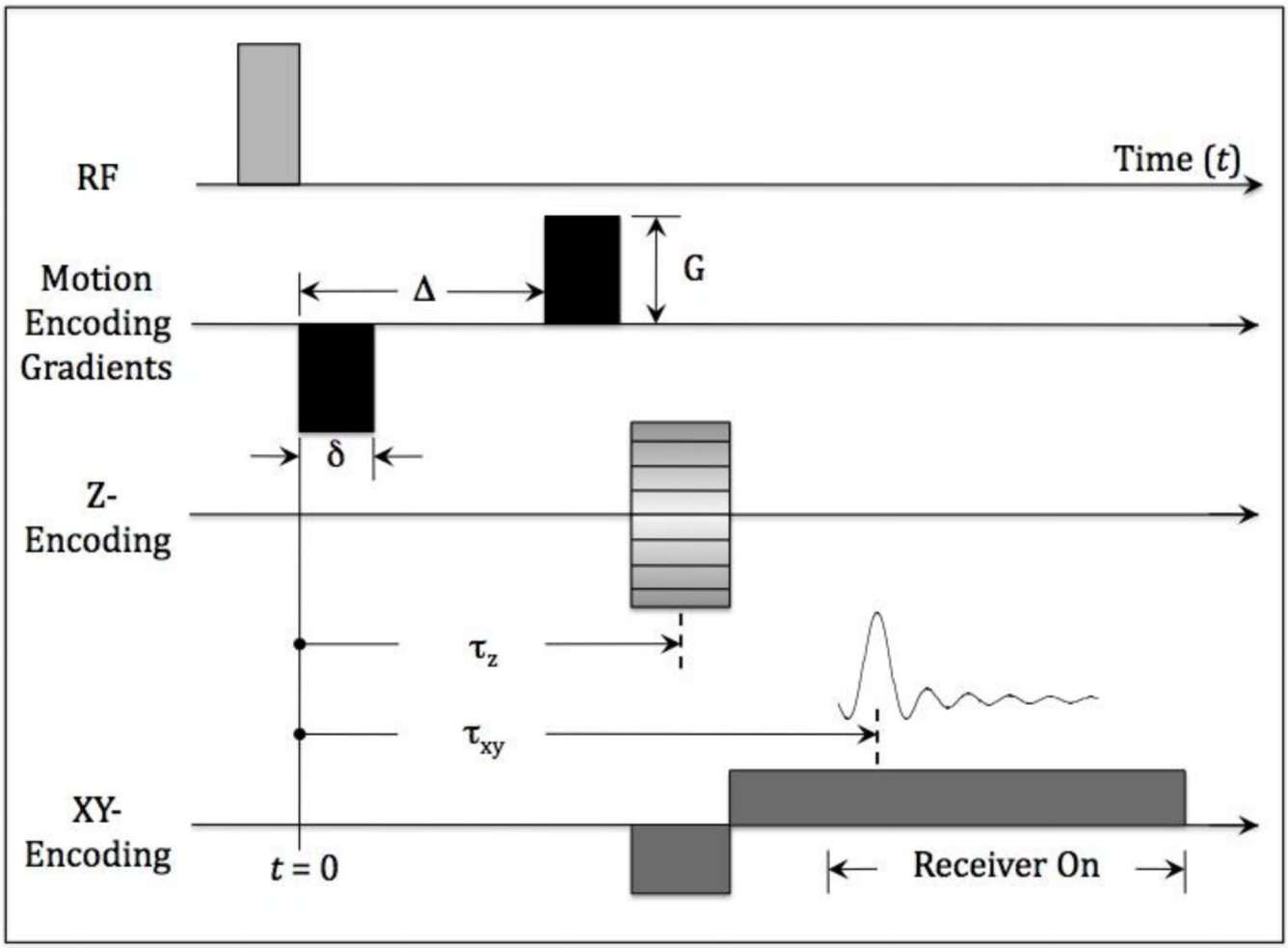

Figure 1.

3D PC-MRI. A square (i.e. non-shaped) radio-frequency (RF) pulse (500 μs long) excites ^{3}He gas using a low flip angle (~10°). Gas motion is then encoded along any orthogonal axis using a bipolar gradient waveform (black) with pulse duration (δ) and separation (Δ) of 300 and 700 μs respectively. Spatial location along the z-axis is registered using a 430 μs phase-encoding pulse, and standard frequency encoding registers radial position in the xy-plane. Phase encoding occurs 1565 μs after gas excitation (τ_z) and an asymmetric gradient echo is refocused after 2339 μs (τ_{xy}).

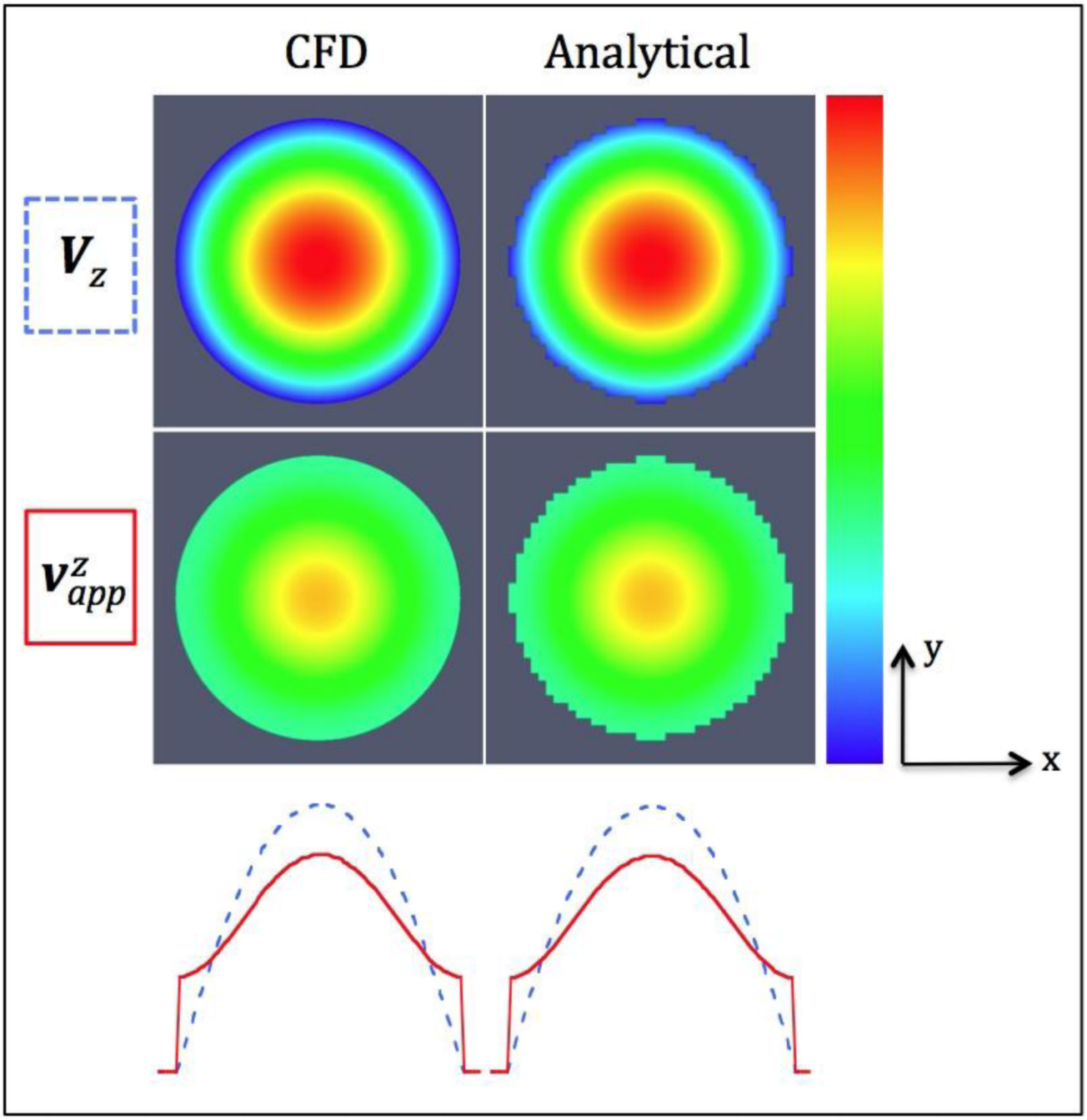

Figure 2.

CFD benchmarking for axial velocity at 1.0 cc s^{-1} in a straight 3.0-mm-diameter tube. $\boldsymbol{V}_z$ is the predicted gas velocity down the tube's symmetry (z) axis when the Navier-Stokes equations are solved using either CFD or analytical methods. Apparent axial velocity ($\boldsymbol{v}_{app}^z$) describes the combined effects of flow and diffusion when measured during PC-MRI in Fig. 1 and ^{3}He gas diffusion is 1.0 cm^2 s^{-1}. Values for $\boldsymbol{v}_{app}^z$ are formulated using either CFD (Eqs. 6–10) or analytical expressions (from prior work[6]). Color in 2D images scales linearly from 0 (blue) to 28.3 cm s^{-1} (red), and 1D profiles show gas velocity across the tube's center along the x-axis.

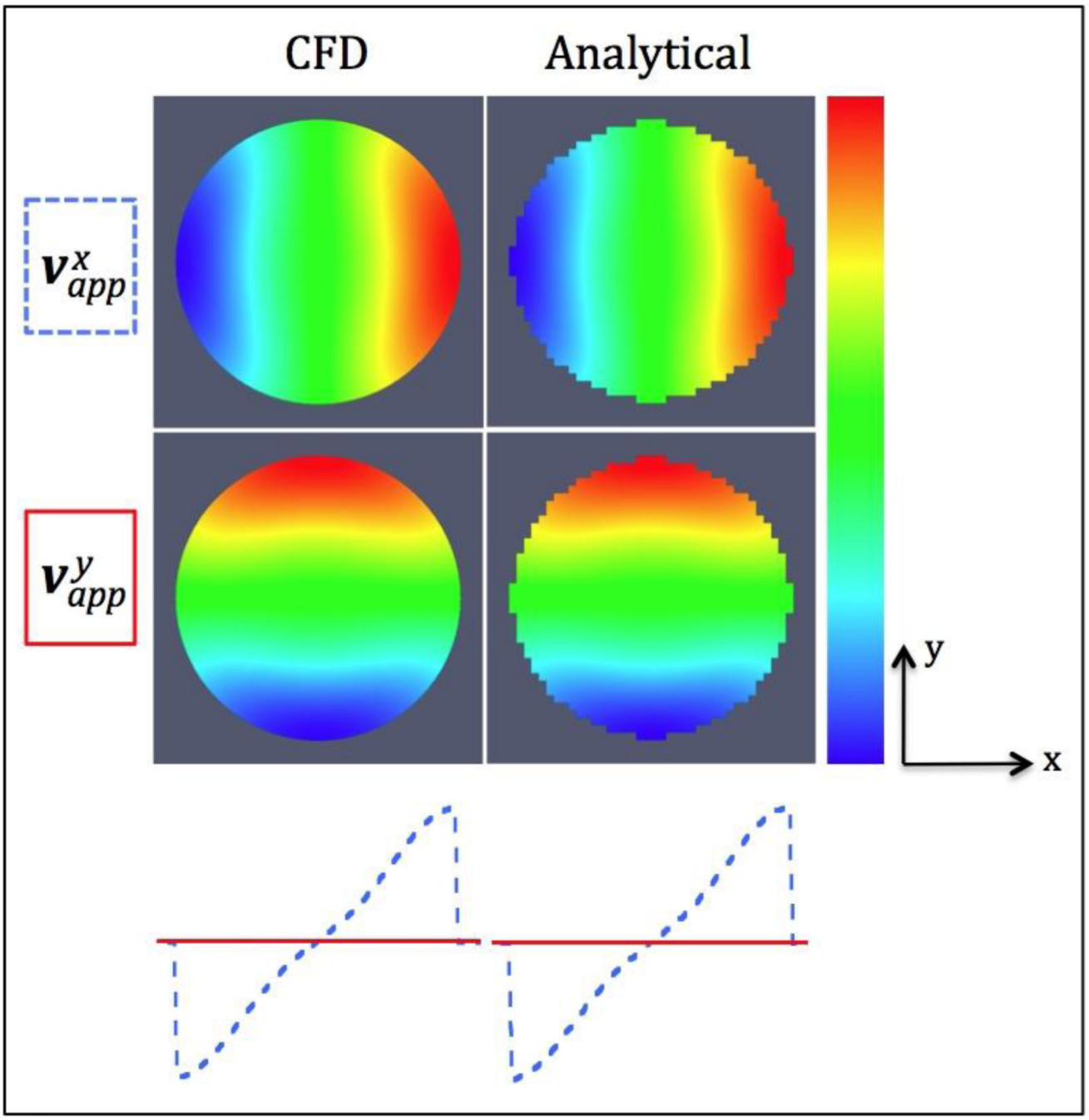

Figure 3.

CFD benchmarking for apparent gas velocity in the x- and y-directions when flow specified in Fig. 2 is measured with PC-MRI shown in Fig. 1. Although the Navier-Stokes equations predict no actual flow structure in these off-axis directions PC-MRI is still sensitive to the Brownian displacements of diffusing gas. In the absence of actual flow these displacements gives rise to apparent velocity values that are predicted from either CFD (Eqs. 6–10) or analytical expressions (formulated using Eqs. 4–5 and the same conditional probability used in prior work[6]). Color in 2D images scales linearly from +15.9 (red) to −15.9 cm s^{-1} (blue), and 1D profiles show gas velocity across the tube's center along the x-axis.

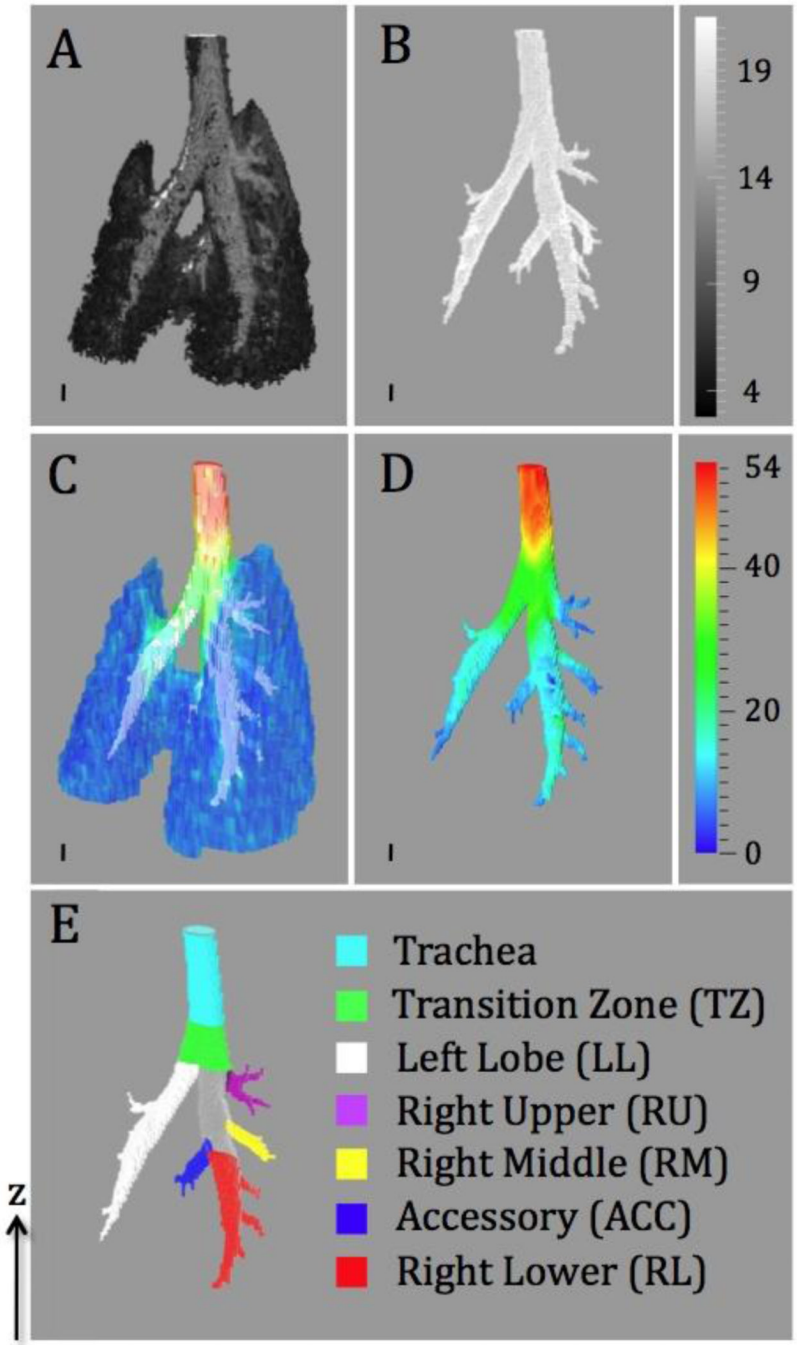

Figure 4.

A) High-resolution ^{3}He MRI displayed using a grayscale that varies with the SNR derived from local MRI signal strength and average noise in magnitude data. B) Segmented airways after a global threshold is used to eliminate MRI signal from gas-filled regions with SNR < 20. C) Overlay showing segmented airways derived from high-resolution MRI and local gas speed measured with PC-MRI. D) Fused MRI data after PC-MRI results are linearly interpolated to fill segmented airways. E) Colorized map showing different airway regions used to measure regional airflow and define CFD boundary conditions. The color scale in C) and D) depicts local gas speed (cm s^{-1}) and the small vertical bar at the lower left corner in each image is 2.0 mm long to highlight z-resolution in PC-MRI.

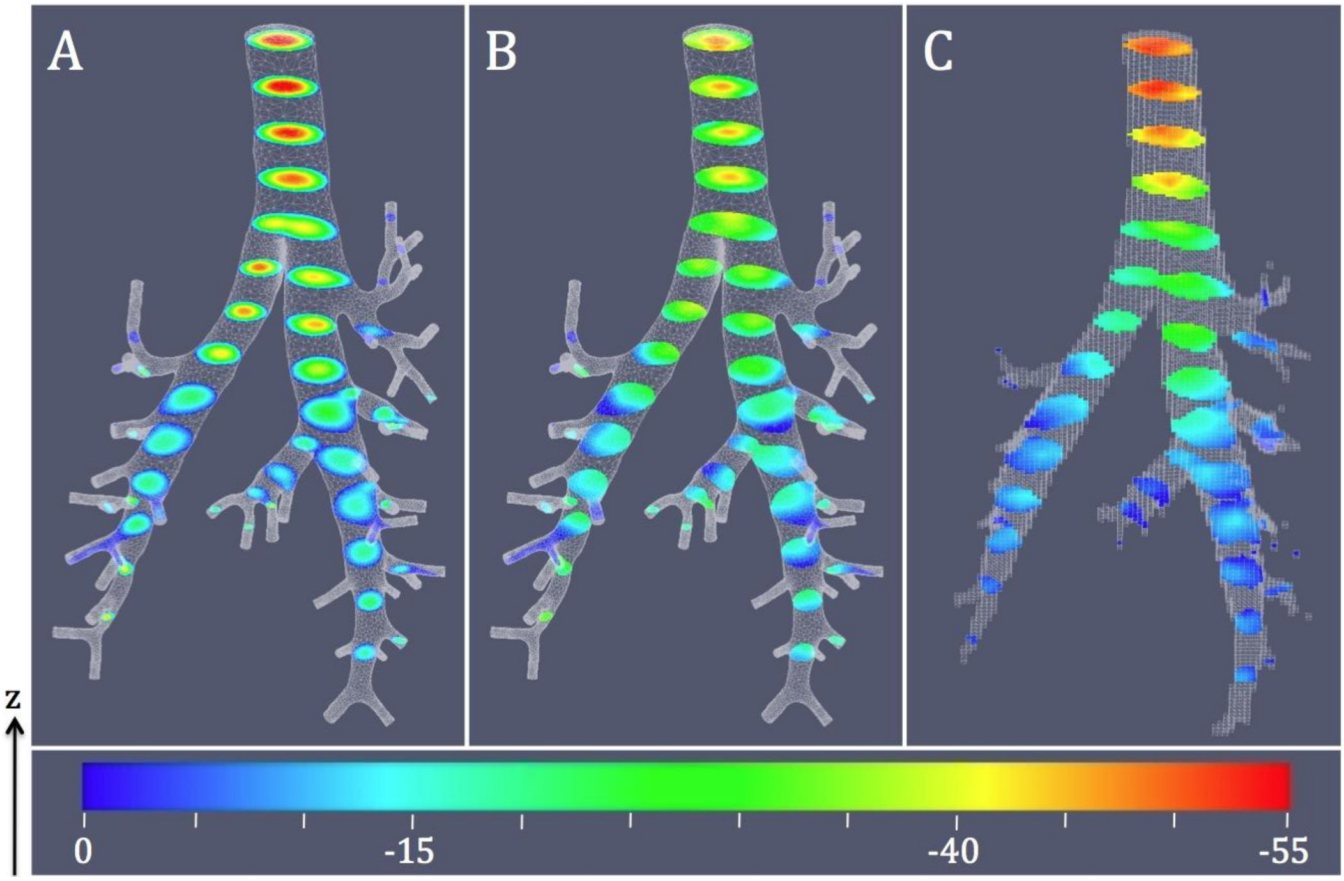

Figure 5.

Inhaled gas velocity along the z-axis. A) Navier-Stokes solution ($\boldsymbol{V}_z$) predicted by CFD, B) simulated values for apparent velocity (v_{app}^{z}), and C) measured values.

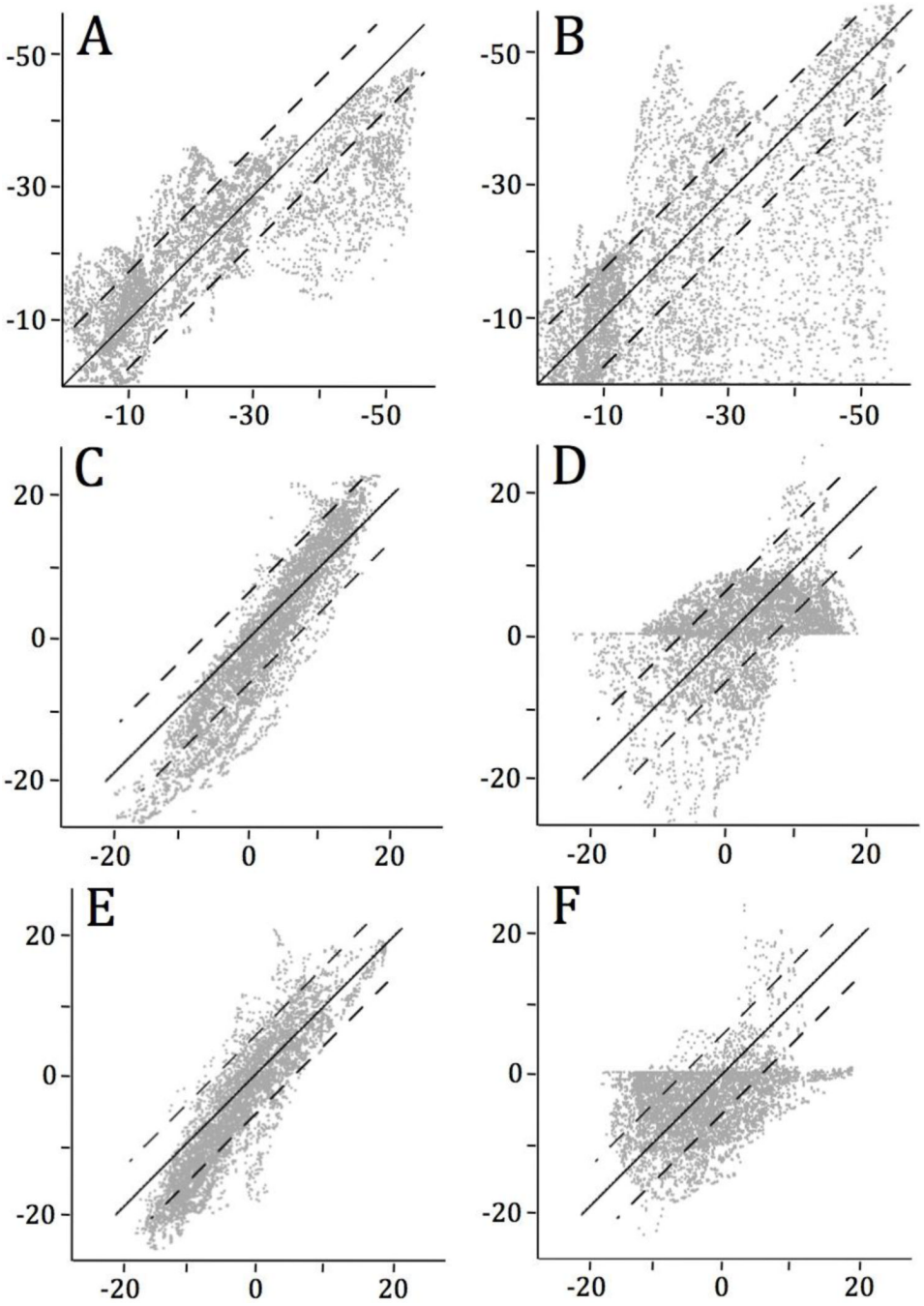

Figure 6.

Regression analysis for comparing CFD and PC-MRI in overlapping regions for all 2D slices shown in Figs. 5, 7, and 8. Each plot shows CFD predictions on the y-axis and use either apparent (v_{app}^{j}) or straight (V_j) velocity values in left or right columns respectively. Plots in the top row show z-velocity components (i.e. j = z), and plots in the middle and bottom show data for x and y. In each plot all velocity units are cm s^{-1}, the solid line represents perfect correlation, and dashed counterparts are plus or minus the mean standard deviation predicted from Eq. 11. Regression results (y-intercept, slope, R^2) are – A) (7.7±0.1, 0.61±0.01, 0.68), B) (6.0±0.3, 0.59±0.01, 0.37), C) (−2.8±0.1, 1.40±0.01, 0.87),

D) (−0.3±0.1, 0.40±0.04, 0.20), E) (−1.5±0.1, 1.27±0.01, 0.83), F) (−3.5±0.1, 0.28±0.01, 0.14).

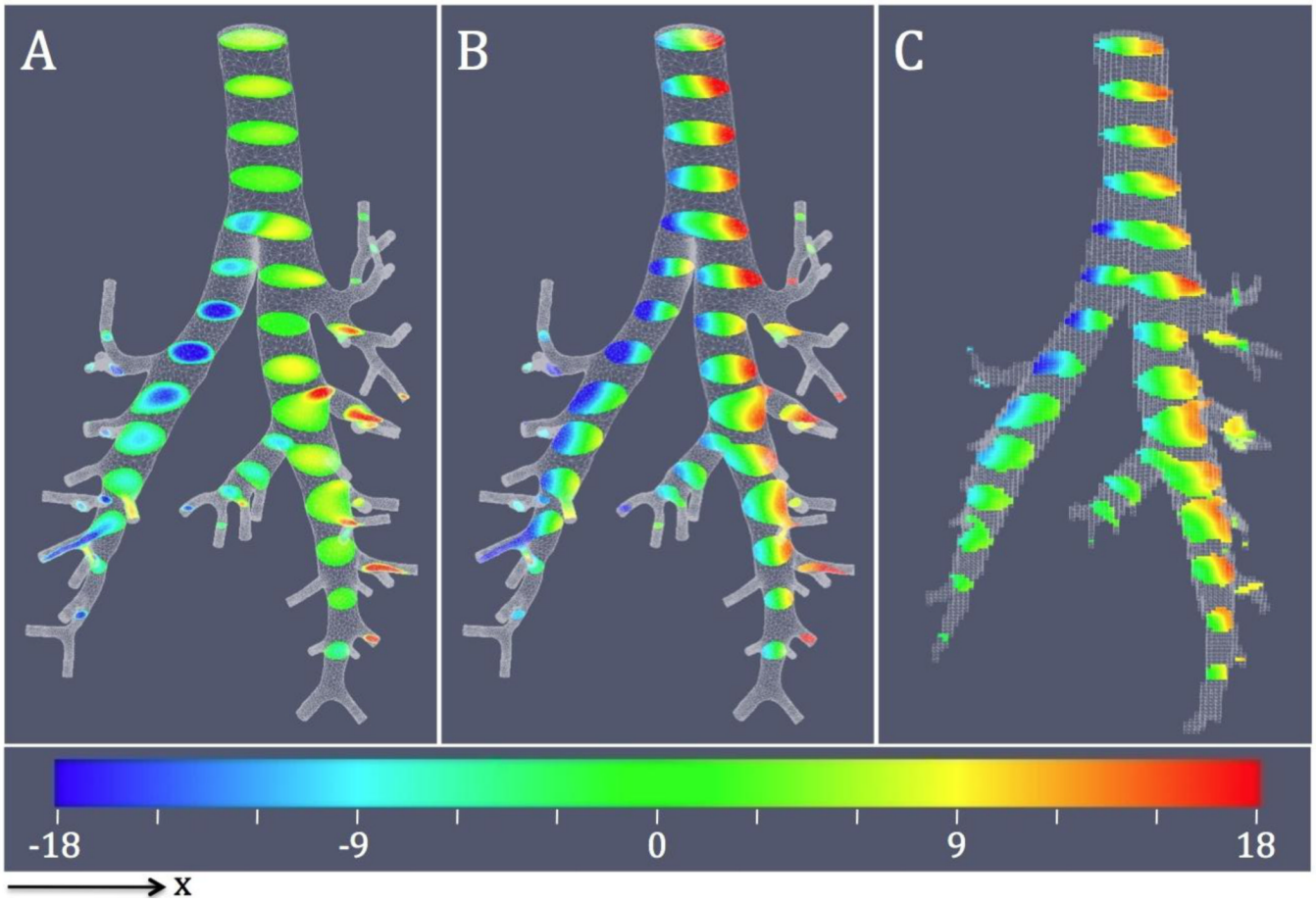

Figure 7.
Inhaled gas velocity along the x-axis. A) Navier-Stokes solution (V_x) predicted by CFD, B) simulated values for apparent velocity (v^x_{app}), and C) measured values.

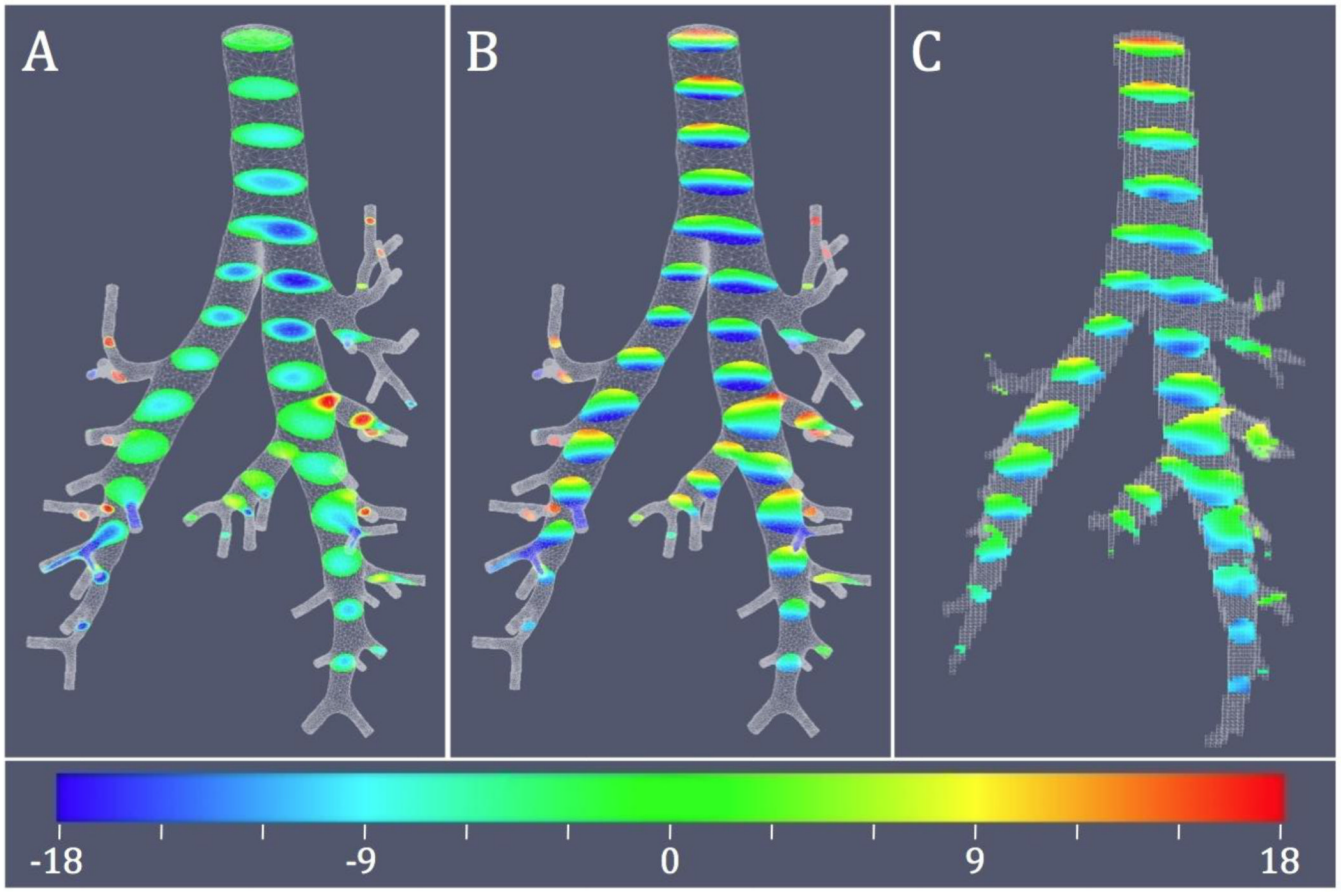

Figure 8.

Inhaled gas velocity along the y-axis (points into page). A) Navier-Stokes solution ($\boldsymbol{V}_y$) predicted by CFD, B) simulated values for apparent velocity ($\boldsymbol{v}_{app}^{y}$), and C) measured values.

Table 1

Regional airflow (cc s^{-1}) measured using ^{3}He MRI. Reported values are the mean and standard deviation from 5 different airway cross-sections. Airway abbreviations are defined in Fig. 4E and shaded table entries highlight data measured for major airways feeding each of the rat's five lung lobes.

	Airway Region						
	Trachea	**TZ**	**LL**	**RU**	**RM**	**ACC**	**RL**
Flow (cc/s)	2.58±0.08	2.25±0.13	0.59±0.05	0.20±0.02	0.17±0.05	0.16±0.02	0.56±0.06
Area(cm^2)	0.058±0.006	0.089±0.009	0.030±0.001	0.019±0.004	0.011±0.004	0.024±0.003	0.065±0.007

Table 2

Percentage of regional airflow measured from numerical predictions of apparent ^{3}He velocity. Reported values are the mean and standard deviation from 5 different airway cross-sections. Airway abbreviations are defined in Fig. 4E and shaded table entries highlight data measured for major airways feeding each of the rat's five lung lobes.

	Airway Region						
	Trachea	**TZ**	**LL**	**RU**	**RM**	**ACC**	**RL**
% Flow	99.6±2.5	103.3±6.6	105.3±2.6	124.8±22.3	108.5±24.9	115.8±23.4	110.0±5.9

J Magn Reson. Author manuscript; available in PMC 2013 August 01.